Cheng, Qiang; Ojanen, Katriina; Diao, Yantao; Kaario, Ossi; Larmi, Martti

Dynamics of the Ammonia Spray Using High-Speed Schlieren Imaging

Published in:
SAE Technical Papers

DOI:
10.4271/2022-01-0053

Published: 08/03/2022

Document Version
Publisher's PDF, also known as Version of record

2022-01-0053 Published 08 Mar 2022

Dynamics of the Ammonia Spray Using High-Speed Schlieren Imaging

Qiang Cheng Aalto University

Katriina Ojanen Energy Authority Finland

Yantao Diao Heze Huaxing Fuel Injector Equipment Co.

Ossi Kaario and Martti Larmi Aalto University

Citation: Cheng, Q., Ojanen, K., Diao, Y., Kaario, O. et al., "Dynamics of the Ammonia Spray Using High-Speed Schlieren Imaging," *SAE Int. J. Advances & Curr. Prac. in Mobility* 4(4):1138-1153, 2022, doi:10.4271/2022-01-0053.

This article was presented at AeroTech, March 15-17, 22-24, 2022.

Received: 19 Dec 2021 Revised: 30 Dec 2021 Accepted: 30 Dec 2021

Abstract

Ammonia (NH3), as a carbon-free fuel, has a higher optimization potential to power internal combustion engines (ICEs) compared to hydrogen due to its relatively high energy density (7.1MJ/L), with an established transportation network and high flexibility. However, the NH3 is still far underdeveloped as fuel for ICE application because of its completely different chemical and physical properties compared with hydrocarbon fuels. Among all uncertainties, the dynamics of the NH3 spray at engine conditions is one of the most important factors that should be clarified for optimizing the fuel-air mixing. To characterize the evolution and evaporation process of NH3 spray, a high-speed Z-type schlieren imaging technique is employed to estimate the spray characteristics under different injection pressure and air densities in a constant volume chamber. Three renewable fuels, including NH3, methanol and ethanol, are investigated to compare the differences in their spray behavior at engine-like conditions. The basic parameters of the spray geometry such as spray penetration, spray cone angle and cross-section area are quantified based on the schlieren images postprocessing. The results show that the spray geometry of NH3 differs from that of the other fuels, which exhibits a longer penetration, larger spray cone angle and cross-section area. Moreover, the NH3 also shows a faster evaporation rate than methanol and ethanol. To extract more information from the spray images, an optical flow algorithm is derived to visualize the velocity field based on the schlieren images. The results indicate that NH3 spray is driven to the spray axis under the effect of the vortices. The vortices are induced by the entrainment of the surrounding gas and act as the driving forces that push the spray plumes towards the axis at the same time. The two vortices of NH3 grow much bigger and stronger and move closer to the spray axis compared to the ethanol and methanol.

1. Introduction

In 2020, 24% of global CO2 emissions comes from transportation through fossil fuel combustion [1]. Road transportation powered by internal combustion engines (ICEs) was by far the main culprit, accounting for nearly 75% of emissions. To become the first climate-neutral continent by 2050, Europe must significantly reduce CO2 emissions from ICE-based transportation in the coming decades. The combustion system, at the heart of ICEs, has a higher optimization potential when powered by carbon-free fuels such as hydrogen (H2) and ammonia (NH3) to mitigate CO2 emissions. The energy vector H2 is a potential enabler of a carbon-free economy. However, issues associated with H2 storage, distribution, and low volumetric energy density (2.9MJ/L at 70MPa) are currently a barrier to its implementation [2]. NH3 offers high energy density (7.1MJ/L), with an established transportation network and high flexibility, which could provide a practical next-generation system for energy transportation, storage, and use for power generation [3], which also offers innovative solutions to sustainability problems within the energy industry.

Reviewing all options of NH3 applications, covering ICE [3, 4, 5, 6], proton-exchange membrane fuel cells (PEMFC) [7, 8], alkaline fuel cell (AFC) [9, 10] and solid oxide fuel cell (SOFC) [11, 12] for power pulsations the ICE has high efficiency and is sufficiently practical [3, 13]. The SOFC scores better in efficiency than the ICE but lacks power density, load response capability and is still too expensive. The ICE is second in efficiency and therefore more efficient than the PEMFC and the AFC (in case these are operated close to maximum power). Furthermore, the ICE is less expensive, more robust with the acceptable power density and load response [14].

NH3 has been successfully operated in SI engine as a mono fuel in 1966 and 1967 by Starkman, et al. [15, 16]. The experiments were carried out in a single-cylinder SI engine with a compression ratio of 6-10 and an equivalence ratio of 0.8-1.4. They conclude that NH3 can be used successfully as a SI engine fuel and presently existing compression ratio. One year later, in 1968, Sawyer, R. et al. [17] started a single-cylinder investigation was conducted to determine the concentration of NOx resulting from the combustion of ammonia and air in a SI engine over a range of fuel-air ratios typical of normal engine operation with ammonia. They found that NOx concentrations exceeded that with hydrocarbons, which imply a different mechanism for NOx formation with ammonia fuel than with hydrocarbons and that some equilibrating processes may take place between combustion and exhaust to reduce otherwise even greater than measured exhaust gas concentrations. In the same year, Starkman, et al. [18] published their new paper to descript the feasibility of the ammonia as a fuel for compression ignition engine. However, the initial studies also indicated that improved combustion with NH3 only can also be achieved by supercharging [19]. They suggested that several plasma jet igniters arranged inside the combustion chamber or plural spark plugs that ignite the ammonia at several points will facilitate ammonia combustion [20]. However, NH3 as the only fuel in SI engines has not been realized at a serious level. Suggestions have been made without any further steps to make this technology feasible in existing vehicles. One possible way to enhance mixing and thereby facilitate the combustion of NH3 is to create turbulence in the combustion chamber. However, a too small swirl does not affect the combustion whereas a too high swirl affects the combustion negatively by blowing the flame out due to slow propagating NH3 flame [21].

One of the most critical problems is that stable, efficient combustion with liquid NH3 is problematic due to extremely high minimum ignition energy (MIE>8mJ) and low flame speed. Furthermore, the use of NH3 in SI-engines is limited by narrow flammability limits, causing incomplete combustion [22]. Thus, fuel additives should be used to solve this problem. Liquid NH3 would reduce the in-cylinder temperature and thereby hinder subsequent turbulence causing deteriorated combustion and misfire. However, most of the mentioned studies on ammonia combustion implemented port-fuel injection for both fuels. Compared to the conventional port fuel injection, GDI injection has potential advantages in high energy density and improved fuel economy due to the flexibility of controlling the fuel-air mixing process [23, 24]. GDI injector directly injects the fuel into the cylinder at high injection pressure to produce finely dispersed droplets, for improving engine performance. Other advantages of GDI technology include better combustion performance, improved fuel economy and higher volumetric efficiency, which have strengthened its scope of application in passenger vehicle segment [25].

High pressure injection systems are widely used in GDI engines to atomize liquid fuel to small droplets. High injection pressure and smaller droplets enable fast engine transient response, good efficiency and reduce emissions [26, 27]. But there is also limitation with using a high injection pressure to atomize liquid fuel. Firstly, the liquid momentum is usually high under a high injection pressure, and the liquid fuel could over penetrate and impinge on the cylinder wall and/or piston surface. This could cause abnormal combustion (such as pool fires), leaving a high level of unburned hydrocarbon and soot emissions [28, 29, 30]. On the other hand, the effects of injection pressure on droplet size reduction decline or even diminish as the injection pressure further increases [31]. Currently, solenoid-actuated inwardly opening multi-hole injectors and piezo-electrically actuated outwardly opening injectors are predominant injectors in GDI engines. Solenoid injectors are more economically viable than piezo injectors because they require lower precision in their manufacturing processes [32, 33]. Piezo injectors, on the other hand, are more attractive because of their sensitive and fast response, which are critical for small quantities or closely spaced multiple injections [34]. The most widely used piezo injector is the outwardly opening hollow cone injector where spray features with visible striations and filaments are observed. Unlike hollow cone pressure-swirl sprays, no collapse arises with the spray development for the outwardly opening hollow-cone piezo injectors [35] and this spray pattern is quite repeatable [36]. The outwardly opening hollow-cone injector also provides sufficient atomization while providing higher flowrates than a multi-hole injector does. Most importantly, with its inherent design characteristics, outwardly opening injectors are immune to fouling and they provide years-long consistent performance. Several studies have been performed on both types of injectors in GDI engines in the past few years. Achleitner et al. [37] investigated a spray-guided combustion system that meets the requirements using a piezo injector. Skogsberg et al. [38] and Wang et al. [39] explored the atomization of sprays generated by a piezo injector. It was shown that a leading-edge vortex is formed at the outer periphery of the spray. The location of the leading-edge vortex depends on in-cylinder pressure. Not many literature piezo injector studies focus on the comparison of spray features using fuels with different physical properties [40].

Even though the spray characteristics of conventional fuels (e.g., gasoline, CH4, etc.) from hollow-cone injector has been extensively studied for many decades. Most of the previous studies on flash boiling spray of gasoline direction injection, however, were conducted on fuel flashing boiling with a multi-hole or single-hole injectors. Few works were done on the flash boiling sprays from non-swirl hollow cone piezoelectric GDI fuel injectors. In this study, experiments were carried out to study the flash boiling spray of a hollow cone GDI piezoelectric injector. Different sets of heating devices were used to ensure that the fuel, injector and ambient temperature are all kept at same value, eliminating the possible variations introduced by temperature difference between the fuel and the environment inside the chamber. By the combination of different temperature (25°C to 125°C) and ambient pressure (1 kPa to 100 kPa), different superheated degrees and different ambient-to-saturation pressure ratios (Pa/Ps) can be achieved. The effects of superheated degree and flash boiling on the spray shape and spray penetration development are analyzed and discussed [41].

In particular, the NH3 as a renewable fuel has been rarely studied its spray characteristics either with multi-hole or hollow-hole injectors. The goal of this experimental study better understanding of the NH3 spray at various injection pressures, chamber densities (pressure), needle lifts (charge voltage). Moreover, the spray characteristics of the ammonia, methanol and ethanol are compared to estimate the effect of physical properties of fuel on the spray behavior.

2. Experimental Setup and Methodology

2.1. Operating Conditions

In the spray measurements, 12 different test points were used. These test points are combinations of four injection pressures 40, 60, 80 and 100 bar and three chamber pressures 5, 10 and 20 bar. The test points were selected to show how the fuel sprays would form using high and low injection and chamber pressures. For each test point, 10 repetitions were made. Ethanol was tested only using the injection pressure of 100 bar and the chamber pressures of 5, 10 and 20 bar. The test points are presented in the experimental matrix below (Table 1).

TABLE 1 Experimental conditions

Cases	Fuel	Injection Pressure	Chamber Pressure	Charge Voltage
Case A: Effect of Pressure ratio	Ammonia	40, 60, 80, 100	5, 10, 20	150
Case B: Effect of Charge Voltage	Ammonia	100	5	120,150,180
Case C: Effect of Fuel Properties	Ammonia, Ethanol, Methanol	100	5, 10, 20	150

2.2. Fuel System

Since the corrosion problem of the NH3 on the copper and its alloys, the fuel system is specially designed for ammonia. The commercial ammonia from Linda is selected, which is stored in a 7.5 bar steel bottle. The ammonia in the bottle is gas phase. However, the desired injection pressure is up to 100 bar, which is liquid phase. Since the phase changing, a huge amount of volume is needed to liquify the gas NH3 to liquid NH3 in the fuel system. Our solution is to implement two piston accumulations (pressure ratio is 1:1) for NH3 pressurizing, as shown in Fig.1. The low pressure NH3 firstly is filled in two piston accumulators. Then close the valve between accumulators and NH3 bottle. The high-pressure nitrogen is used to drive the piston moving and pressurizing the NH3. Since the liquification of the NH3, there is a huge volume loss during the pressurization. Therefore, the two valves between two piston accumulators should be manually closed and opened several times to let more pressurized ammonia enter the system, until the whole system filled with liquid ammonia. The pressure of the ammonia is controlled by nitrogen regulator.

A hollow cone piezoelectric injector was used to inject fuels into a constant volume chamber. The hollow cone piezoelectric injector is a commercial gasoline direct injection injector which is made by Siemens VDO Automobile. It can

FIGURE 1 Schematic of the experimental setup.

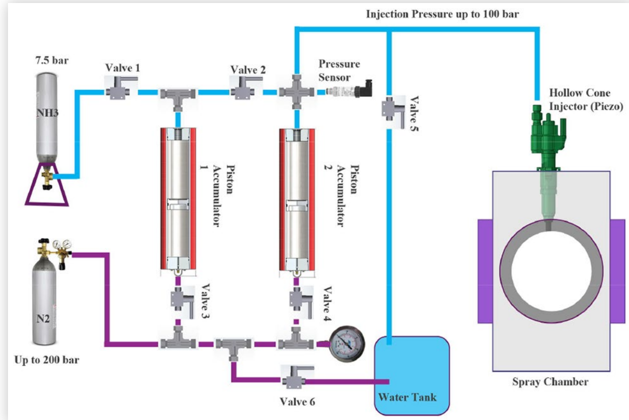

use rail pressures up to 200 bar. The injector used in the measurements is shown in Fig.8. The advantage of this piezo injector is that the dynamics response is much faster than the other solenoid injectors. The needle lift is depending on the voltage and the charge fed into the piezoelectric stack, which means high voltage leads to larger needle lift. In the present study, the injector charge voltage is 150 V.

FIGURE 2 Hollow cone piezo injector.

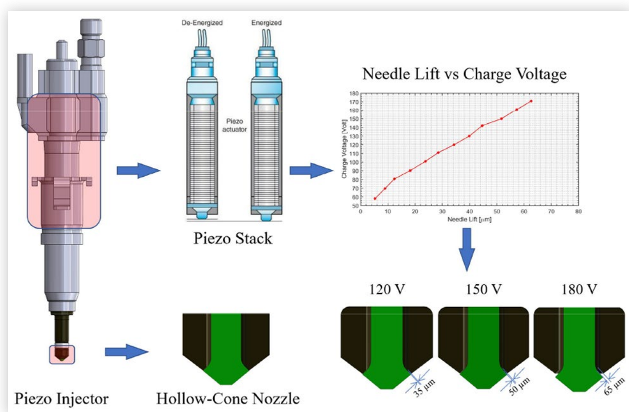

2.3. Constant Volume Spray Chamber

A constant volume spray chamber is applied to create the engine-like conditions for spray study. Two borosilicate windows (100mm of diameter) in horizontal direct are allowed the light accessible. The maximum gas pressure allowed in the chamber is 35 bar. The temperature and pressure sensors are located on the side of the spray chamber. During the experiments, the chamber is filled with nitrogen with desired pressure. In this study, the pressures are set to 5 bar, 10 bar and 20 bar. The temperature inside the chamber is the ambient temperature, approximately 24 °C. The exhaust line of the spray chamber consists of a safety valve and release valve, which are used to avoid over pressure limits and release the residual gas in the chamber. The control of the measurements setup such as triggering the fuel injector and the high-speed camera was operated using LabVIEW. Driven CompactRIO DI Driver Module was used to trigger the injector. During the measurements, the pressure and temperature inside the chamber and the injection pressure were measured. This information of the sensors and the calculated chamber density were shown on the LabVIEW interface. The control system is shown in Fig.7 in red.

2.4. High-Speed Schlieren System

Fig.2 shows the schematic of the optical system. A traditional high-speed Z-type schlieren imaging technique is applied for NH3 spray visualization. The schlieren imaging setup consists of an LED light source, pinhole, two parabolic mirrors, a knife edge, an iris, and a Phantom V2012 high-frame-rate Complementary Metal-Oxide Semiconductor (CMOS) camera. The spot light emitted from the LED source (green light with wavelength 532 nm) is collimated by one of the parabolic mirrors (focal length 609,6 mm) and sent through the spray chamber. The other parabolic mirror (focal length 762 mm) setup identical to the collimating mirrors focuses the light onto the CMOS chip of the camera. An iris instead of the knife edge is adopted block part of light to create schlieren image. The high-speed camera is synchronized by the injection signal. Images are collected during whole injection process until the spray touch the edge of the window. The frame rate is fixed at 34 kfps with 1 µs exposure time, the resolution of the image is 768×768 pixles.

FIGURE 3 The sketch of the high-speed schlieren system

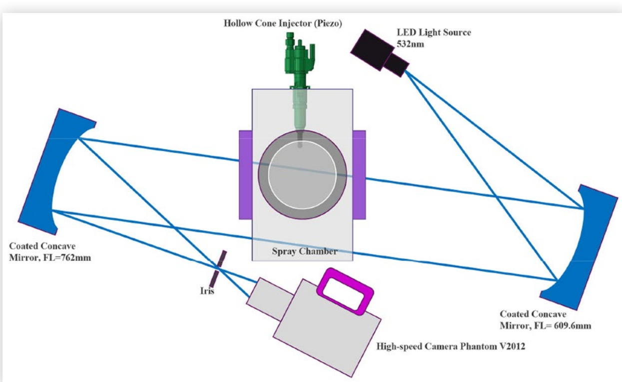

2.5. Image Postprocessing

To process these images, the frames before the appearance of the spray event are averaged to provide a background image which all subsequent images are subtracted by. The subtracted images are converted to binary images based on adaptive thresholding approach. According to the modified binary images, the boundary of the spray can be recognized and the spray geometry parameters such as penetration, width and area can be calculated. The detailed image post-processing approach can be seen in Fig. 4.

FIGURE 4 Image post-processing

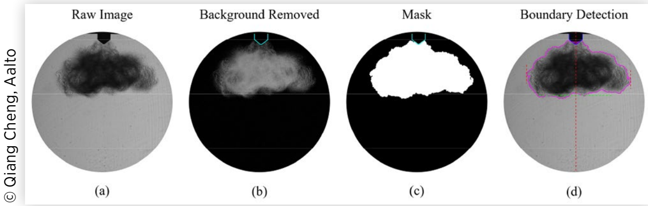

2.6. Optical Flow Method

To further obtain more information of ammonia spray in the flow field, an optical flow method is introduced to calculate the velocity distribution of the spray with schlieren images. The optical flow method has been developed for extraction of high-resolution velocity fields from various images of continuous patterns from flow visualization images obtained in laboratories to cloud and ocean images taken by satellites/spacecraft [42, 43, 44, 45, 46, 47]. The rational foundation for the application of the optical flow method to fluid flow measurements is the quantitative connection between the optical flow and the fluid flow velocity for various flow visualizations. Liu and Shen [48] have derived the projected motion equations for various flow visualizations including laser-sheet-induced fluorescence images, transmittance images of passive scalar transport, schlieren, shadowgraph and transmittance images of density-varying flows, transmittance and scattering images of particulate flows, and laser-sheet-illuminated particle images. Further, these equations are recast into the physics-based optical flow equation in the image plane. Physically, the optical flow is proportional to the light-ray-path-averaged velocity of fluid (or particles) weighted in a relevant field quantity like dye concentration, fluid density or particle concentration. The optical flow method has been used to study the flow structures of Jupiter's Great Red Spot

FIGURE 5 Block diagram of the optical flow method for schlieren-based spray velocity field

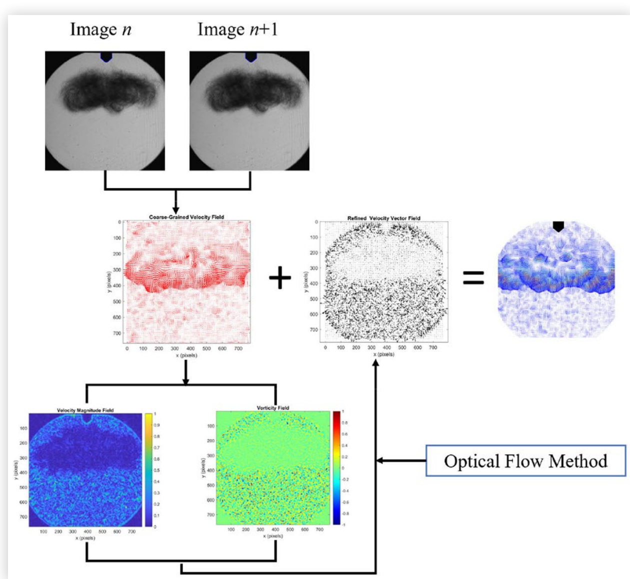

(GRS), impinging jets, and laser-induced underwater shock wave [49, 50, 51, 52]. A mathematical analysis of the variational solution of the optical flow and an iterative numerical algorithm are given by Wang et al. [53]. The systematic error analysis of the optical flow method in velocity measurements is given by Liu et al. [47] in comparison with the well-established cross-correlation method in particle image velocimetry (PIV).

3. Results and Discussion

3.1. Effect of the Injection Pressure on the Ammonia Spray

The effect of the injection pressure on the spray characteristics has been extensively investigated. The majority of these studies involve the experimental and semi-experimental equations which estimate the penetration length, spray area, spray cone angle as a function of velocity, ambient density and the orifice geometry. The experimental and numerical results show that increasing the injection pressure leads to increasing the turbulence of the fuel flow and consequently the velocity of the liquid jet at the outlet of the orifice gets higher, which generate a longer spray penetration, larger spray area. Fig. 6 shows the spray evolution at various injection pressure (40, 60, 80 ,100 bar) and constant chamber pressure 10 bar. It shows that the higher injection pressure leads to a longer spray penetration and larger spray area. It can be observed that as the pressure increases, the edge of the spray becomes more unstable. Moreover, increasing the injection pressure also improves the evaporation rate, which can be related to the higher injection pressure enhancing the ammonia-air entrainments and generating finer droplets.

FIGURE 6 Evolution of the ammonia sprays at an injection pressure of 40, 60, 80, and 100 bar and a chamber pressure of 10 bar

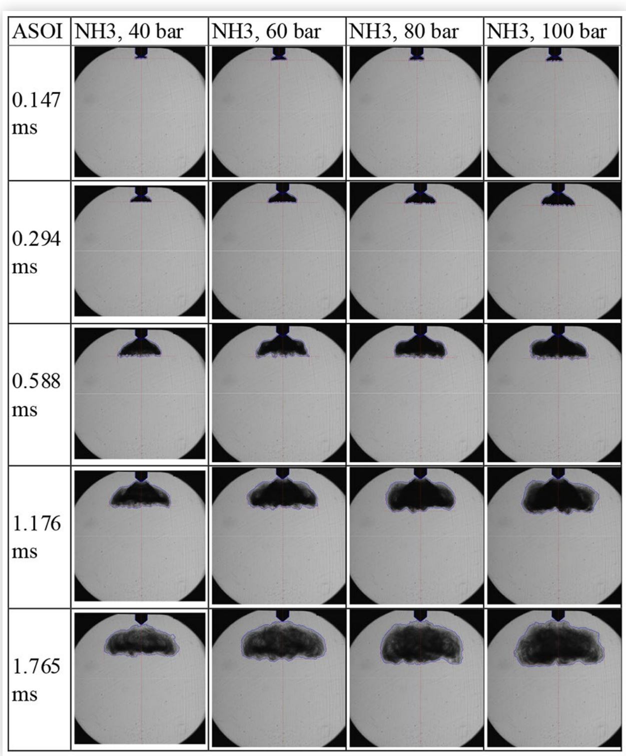

3.1.1. Spray Penetration

Fig. 7 (a)-(c) shows the effect of the injection pressure on the penetration at various chamber pressure (5 bar, 10 bar and 20 bar). It can be seen that the higher injection pressure leads to longer penetration due to higher injection pressure providing higher momentum. At lower chamber pressure as shown in Fig. 7 (a), a significant transition between momentum-driven propagation and free moving propagation can be observed after injector valve closing. This is because during injector valve opening, the high-pressure ammonia leaves from the nozzle at a very high velocity. However, after the injector valve closed, the velocity of the spray gradually decreased due to the absence of high-velocity fresh ammonia. The significance of velocity transition is decreased with the increase of the chamber pressure. The injection pressure is affecting on the penetration more during

FIGURE 7 The spray penetration at an injection pressure of 40, 60, 80 and 100 bar with a chamber pressure of 5, 10 and 20 bar.

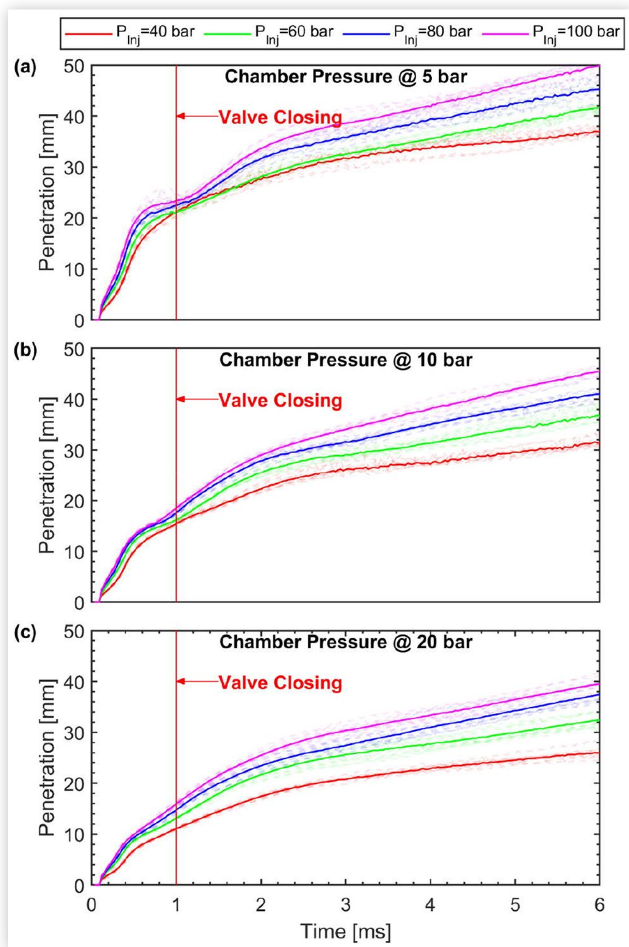

the early stage of the penetration and less during the later stage of the penetration. In the later stage, the spray penetrates slower. The higher injection pressure is causing higher spray momentum and higher mixing efficiency. This means that the air and fuel mixing rate can be increased by increasing the injection pressure.

3.1.2. Spray Area Fig. 8 (a)-(c) shows the influence of the injection pressure on the spray area. As expected, increasing the injection pressure also leads to a larger spray area. This is because the increase of the injection pressure leads to a higher momentum, which not only increases the velocity in the axis direction but also radial directly. This is because the nozzle geometry of the injector is with a 90° umbrella angle. Therefore, increasing the injection pressure results in a simultaneous increase in penetration and injection with, as well as the spray area. The significant increase of the spray area corresponds a better fuel-air mixing.

FIGURE 8 The spray area at an injection pressure of 40, 60, 80 and 100 bar with a chamber pressure of 5, 10 and 20 bar.

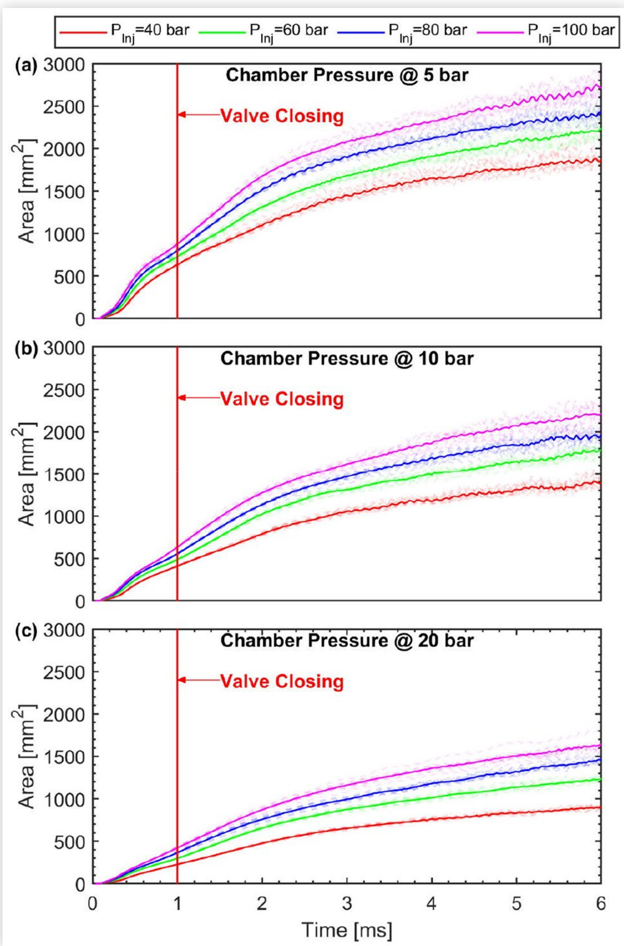

3.1.3. Velocity Field Fig.9 illustrates the velocity field of the ammonia spray at an injection pressure of 40, 60, 80, and 100 bar and the chamber pressure of 10 bar. It should be noted that at the beginning of the injection, the spray shows very high optical density, therefore, the optical method couldn't calculate the velocity accurately. In this study, we start to calculate the velocity field at 0.588 ms after the start of injection (ASOI). It can be seen that the high velocity can be observed both near the nozzle and spray tip. during the injection valve is open. This is because the high-velocity ammonia is injected out from the nozzle enhance the momentum of the spray. Unfortunately, since the dense region at the centre of the spray, the optical flow method couldn't predict the velocity properly. After the injector valve closed, the spray near the nozzle shows very low velocity due to the absence of the ammonia after valve closing. It is clearly shown that the increase of the injection pressure enhances the turbulence in the spray. This is because by having an increase in the injection pressure, the ammonia-air entrainment is more complex and intense. The turbulence intensity is stronger, the spray's atomization degree increases, the droplet diameter of the spray is smaller, and the effect of increasing the momentum is weakened.

FIGURE 9 Velocity field of the ammonia spray at an injection pressure of 40, 60, 80, and 100 bar and a chamber pressure of 10 bar

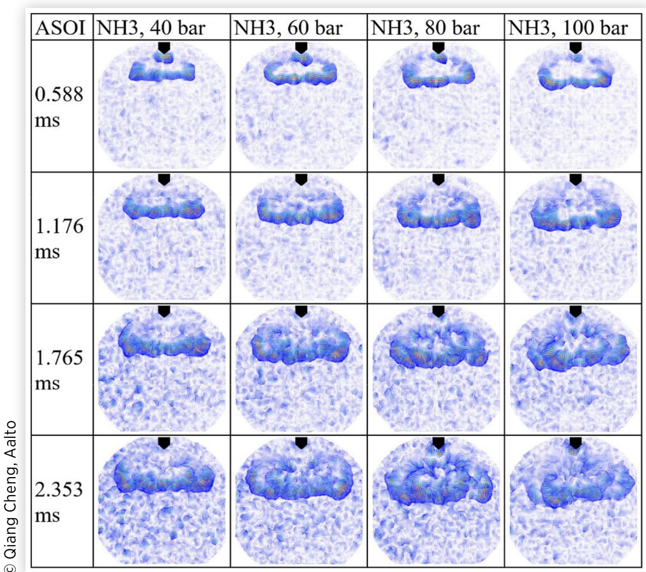

3.2. Effect of the Chamber Pressure on the Ammonia Spray

Fig. 10 shows ammonia spray evolution at the different chamber pressures of 5, 10 and 20 and an injection pressure of 100 bar. Compared to injection pressure, the effect of chamber pressure on spray evolution is significant and more straightforward. It can be seen that the effect of increasing chamber pressure is markedly evident with a large reduction in spray width and spray penetration length. The images show clearly that the spray penetration and width get shorter and narrower with an increase in chamber pressure. Effectively, increased chamber pressure gives rise to higher gas density, which is what spray droplets experience. More specifically, as

FIGURE 10 Evolution of the ammonia sprays at a chamber pressure of 5, 10 and 20 bar and an injection pressure of 100 bar and.

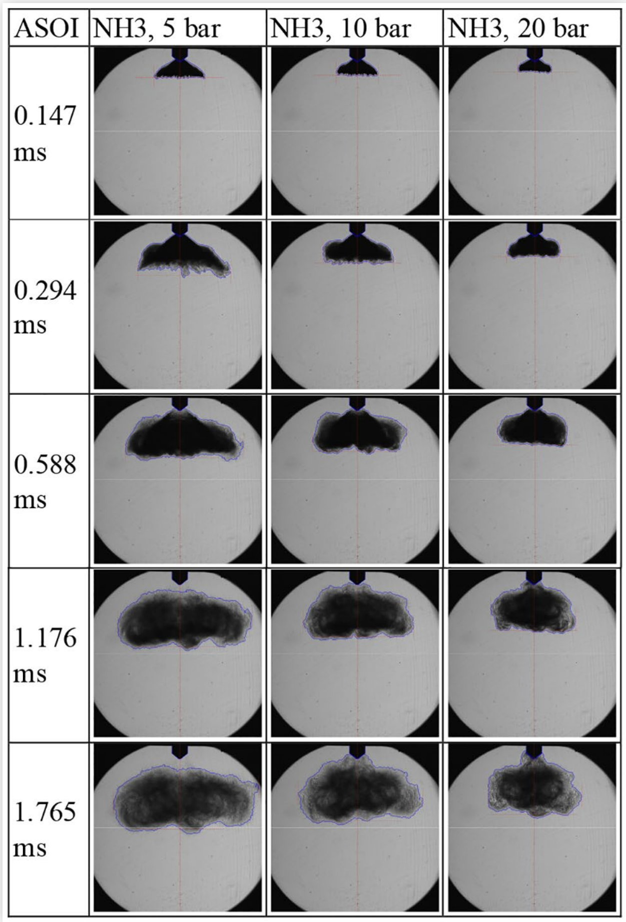

droplets emerge from the nozzle, they face a considerably denser gaseous medium that causes droplets to rapidly decelerate. This sudden spray velocity reduction can lead to droplet coalescence and formation of large diameter droplets. Another effect of velocity reduction would be hindering the possibility of the secondary break-up, which is directly dependent on the relative velocity between the droplets and the surrounding air.

3.2.1. Spray Penetration Fig. 11 (a)-(c) shows the effect of the ambient chamber pressure (5, 10, 20 bar) on the spray penetration at various injection pressures (60, 80 and 100 bar). It can be seen that increasing the chamber pressure dramatically decreases the spray penetration. As shown in Fig. 11, with the increase of the ambient chamber pressure, more liquid ammonia ligaments and droplets can be observed in dense region at the higher ambient pressures compared with the lower ambient pressure cases. The explanation behind this phenomenon is that the growing ambient pressure increased the density of the ambient air, thus the air drag force is strengthened to promote the breakup of the liquid jet. However, the higher air drag force leads to an intense ammonia-air entrainment due to the aerodynamic shear force squeezing the protruding liquid column and causing the liquid dispersion from the centre to the periphery [55]. The development of the spray is strongly frustrated, and the penetration length is shorter under the higher ambient pressure. It is also shown that increasing the injection pressure has a similar spray penetration trend.

FIGURE 11 The spray penetration of ammonia at a chamber pressure of 5, 10 and 20 bar with an injection pressure of 60, 80 and 100 bar

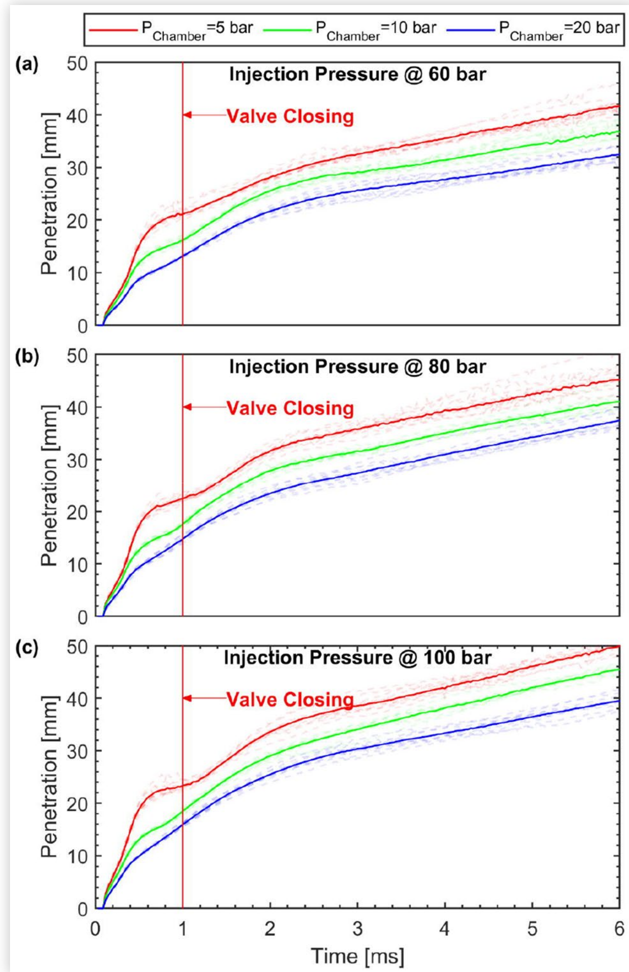

3.2.2. Spray Area Fig. 12 (a)-(c) depicts the effect of the chamber pressure on the spray area at various chamber pressures of 5, 10 and 20 bar and injection pressure of 60, 80, and 100 bar. As aforementioned explanations, increasing the chamber pressure results in a higher chamber density, which leads to a higher air drag force and larger resistance for spray propagation. Therefore, the spray shows reduction both in axial and radial direction, resulting in a smaller area. The phenomenon can be observed at all injection pressures. The results indicate that when using late injection timing in the ammonia engine, ammonia-air mixture exhibits more stratification than earlier injection timing.

3.2.3. Velocity Field As previous explanations, the higher ambient chamber pressure leads to a shorter spray penetration and smaller spray area due to the larger air drag force and resistance for spray propagation. This also leads to

FIGURE 12 The spray area of ammonia at a chamber pressure of 5, 10 and 20 bar with an injection pressure of 60, 80 and 100 bar

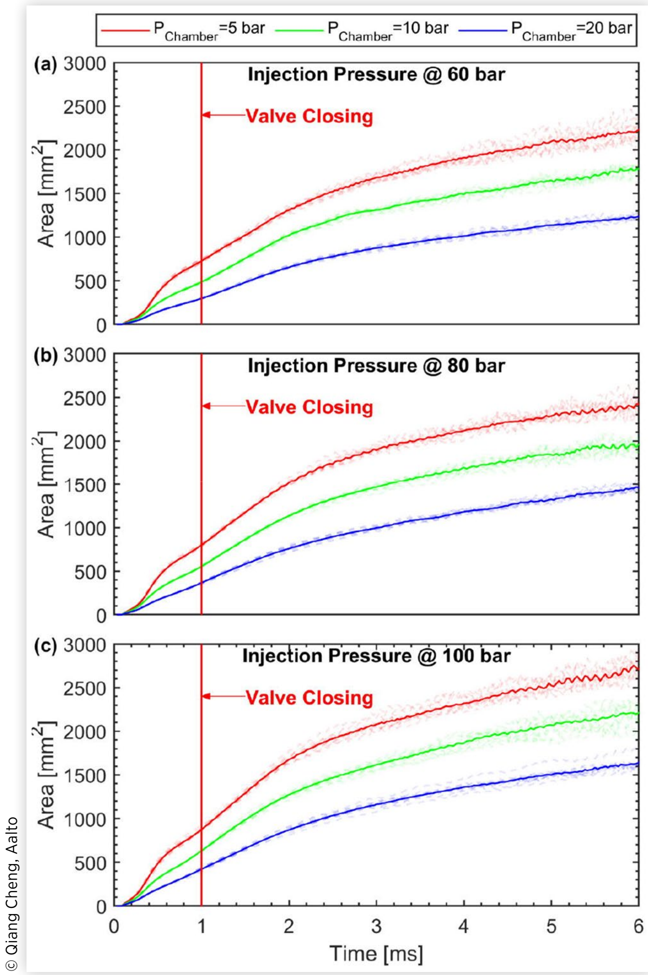

FIGURE 13 Velocity field of ammonia at chamber pressure of 5, 10 and 20 bar with an injection pressure of 100 bar

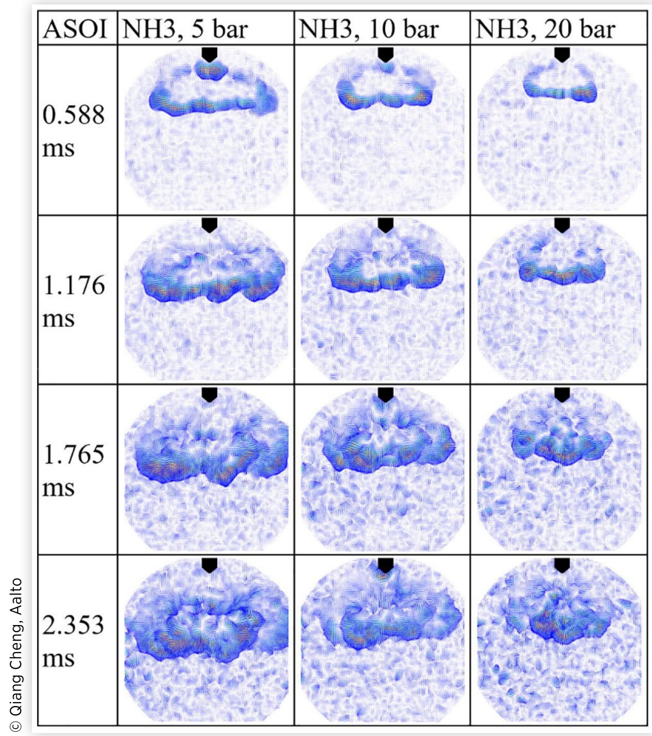

a denser region near the nozzle. Fig. 13 demonstrates the velocity field of the ammonia spray at various chamber pressures of 5, 10, and 20 bar and an injection pressure of 100 bar. It is clearly observed that before the injector valve closing (0.588 ms ASOI), the optical flow method for velocity estimation at a chamber pressure of 20 bar is failed due to the thick optical density, which couldn't recognize the flow gradient in the spray. Moreover, the spray at a higher ambient chamber pressure displays a low velocity and smaller area. After the injector valve closing, the ammonia spray at a lower chamber pressure exhibits higher velocity and more turbulence due to less air drag force and lower resistance for the spray propagation.

3.3. Effect of the Pressure Ratio on the Ammonia Spray

According to previous analysis, the spray characteristics are determined by both injection pressure and ambient chamber pressure. To gain a further insight into this combinative effect on the spray behaviours, the effect of the pressure ration on the ammonia spray is discussed in this section.

Fig. 14 shows the evolution at various pressure ratios of 4 (40/10 and 80/20) and 8 (40/5 and 80/10). It can be observed that at the same pressure ratio, the spray at lower injection pressure and chamber pressure exhibits sharper edges compared to the higher injection pressure and chamber pressure. This implies that the higher air density in the chamber creates more resistance to obstruct the spray evolution. Moreover, the spray at lower pressure ratio shows shorter spray penetration and smaller spray area.

3.3.1. Spray Penetration Fig. 15 shows the effect of the pressure ratio on the ammonia spray penetration. Even though, some of the studies on gas jet observed that the penetration curves fall together for each pressure ratio [56]. However, the ammonia spray shows totally different characteristics. It can be seen that the ammonia spray exhibits the non-linear properties even after at the beginning of injector valve opening. This phenomenon especially at higher injection pressure and larger pressure ratio. Later in the injection process, the jet tip velocity continually drops, and spray shows more linear properties. The differences between the ammonia spray and gas jet can be attributed to the phase transition of ammonia from liquid to vapor.

3.3.2. Spray Area Fig. 16 depicts the spray area of ammonia at various pressure ratios of 4 (40/10 and 80/20) and 8 (40/5 and 80/10). Compared to the spray penetration at various pressure ratios shows different trends, the spray area curves at the same pressure ratio shows a similar trends to

FIGURE 14 Evolution of the ammonia sprays at various pressure ratios of 4 (40/10 and 80/20) and 8 (40/5 and 80/10)

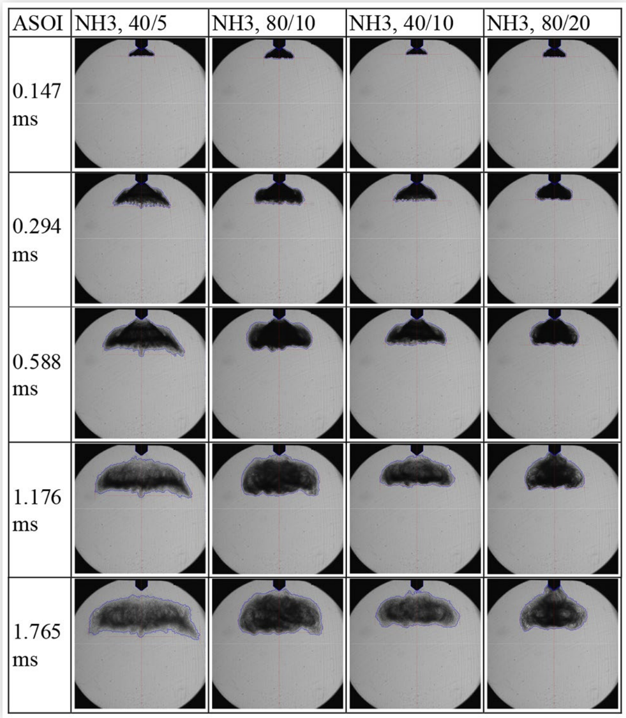

© Qiang Cheng, Aalto

FIGURE 15 The spray penetration of ammonia at various pressure ratios of 4 (40/10 and 80/20) and 8 (40/5 and 80/10)

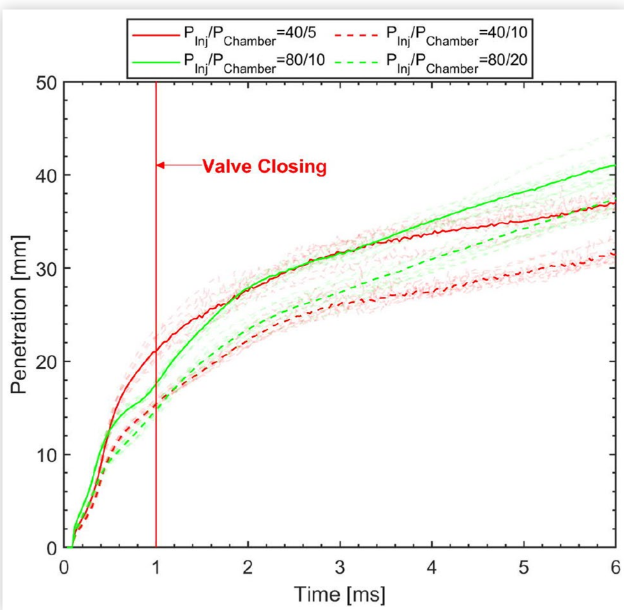

© Qiang Cheng, Aalto

each other. It can be seen that more differences take place during the injector valve opening. This is because during the injector valve opening, the ammonia spray is driven by the momentum of the high-pressure ammonia from the nozzle. Thus, the spray behaviour is dominant by the injection pressure. However, after the injector valve closing, the spray propagation is determined by the air dray force.

FIGURE 16 The spray area of ammonia at various pressure ratios of 4 (40/10 and 80/20) and 8 (40/5 and 80/10)

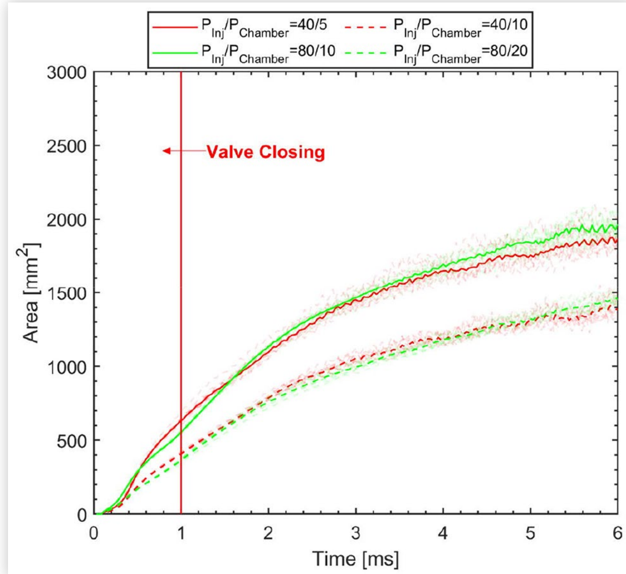

© Qiang Cheng, Aalto

The combinative effect leads to the spray area similar after the injector valve closing.

3.3.3. Velocity Field

Fig. 17 demonstrates the velocity field of the ammonia spray at various pressure ratios of 4 (40/10 and 80/20) and 8 (40/5 and 80/10). It is clearly observed that before the injector valve closing (0.588 ms ASOI), the optical flow method for velocity estimation at 20 bar is failed due to the thick optical density, which couldn't recognize the flow gradient in the spray. Moreover, the spray at a higher ambient chamber pressure displays a low velocity and smaller area. At the same pressure ratio, the lower injection pressure and chamber pressure shows more turbulent flow close to the boundary of the spray. On contrary, more turbulence can be observed in the inner region of the spray at the higher injection and chamber pressure. This is because the higher chamber density creates more obstacle for the spray propagation and induces more turbulence in the inner region of the spray.

3.4. Effect of Needle Lift on the Ammonia Spray

As shown in Fig. 2, by increase the charge voltage of the piezo injector leading to a larger needle lift. This can result in a more amount of ammonia injected out from the nozzle. As shown in Fig. 18, the ammonia spray from a larger needle lift shows a longer spray penetration and larger area, as well as a larger dense region. The reason for this phenomenon may be that the injectors with a larger needle lift has a slower pressure buildup. In addition, they also have larger spray cone angles and spray angles at the beginning. Therefore, the momentum of the spray with a larger needle lift at the beginning is larger than a smaller needle lift injector. However, after the injector valve closing, the momentum of the injectors with larger needle lift starts to increase per unit time, and the increase in

FIGURE 17 Velocity field of ammonia at various pressure ratios of 4 (40/10 and 80/20) and 8 (40/5 and 80/10)

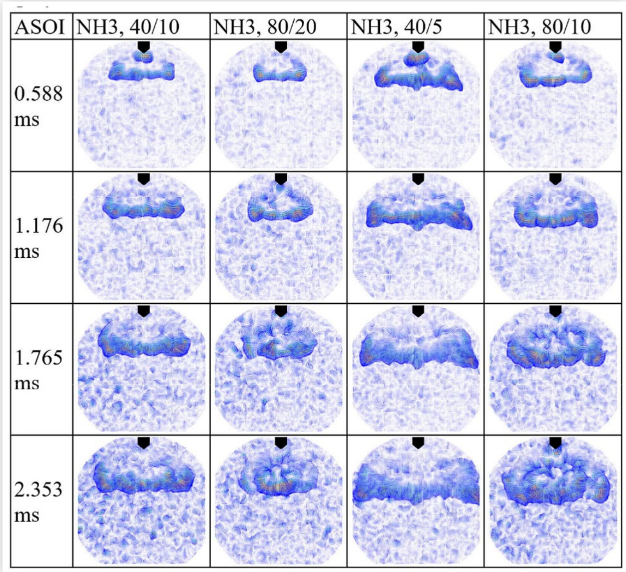

the momentum of the smaller needle lift becomes smaller. With the time going on, the injection rate, spray angle, and spray cone angle are gradually stabilized, and the penetration of the injectors with the larger needle lift gradually surpasses the smaller needle lift nozzle. Therefore, the injectors with larger needle lift have a larger spray penetration and spray area. Fig.18 shows that the spray penetration and spray area with needle lift of 60 μm is much larger than those with the needle lift of 35 60 μm.

3.4.1. Spray Penetration

As aforementioned explanations, the increase of the charge voltage (from 120 V to 180 V) leads to a larger needle lift (from 35 μm to 60 μm), resulting in a larger amount of liquid ammonia injection (larger injection rate). The larger injection rate creates higher momentum during the injection, which results in longer injection penetration. Fig. 19 (a)-(c) shows that the spray penetrations are increased with the increase of the needle lift at all tested injection pressure (60, 80, and 100 bar) and a constant chamber pressure of 5 bar. It is worth noting that at the beginning of the injection (ASOI < 0.5 ms) all the sprays exhibit similar behaviour. This might be related to the initial flow velocity of the spray. Since piezo stack has extremely mechanic response rate, the ammonia is injected out immediately after the piezo stack is energized (< 0.1 ms according to the image detection for all charge voltage). During the valve opening time, the momentum driven ammonia spray has a similar initial velocity and momentum. However, with the time going on, the higher charge voltage leads to a larger stabilized needle lift, and more liquid ammonia injected out. This results in a larger momentum ammonia injected out due to the higher injection rate. Moreover, a larger needle lift also reduce the resistance in the nozzle, which might increase the initial velocity when the injection valve fully open.

FIGURE 18 Evolution of the ammonia sprays at various needle lifts of 0.35, 0.50 and 0.65 μm

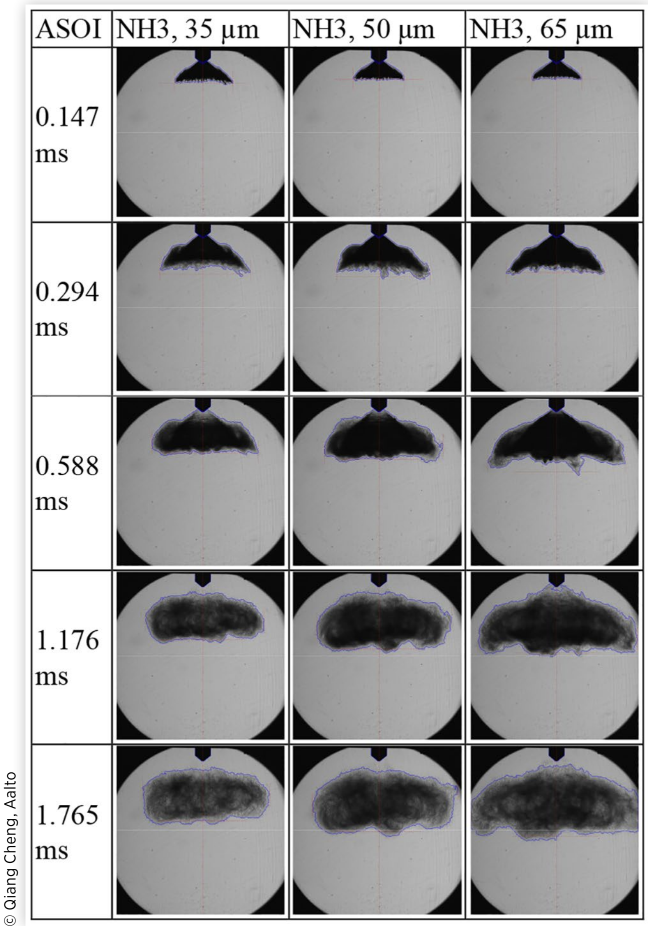

3.4.2. Spray Area

Fig. 20 (a)-(c) illustrates the spray area of ammonia at various needle lifts of 0.35, 0.50 and 0.65 μm. It is shown that the increase of the needle lift dramatically enlarges the spray area at all tested injection pressures. A similar spray area behavior can be observed at the beginning of the injection (ASOI < 0.5 ms) all the sprays. As explained in section 3.4.1, this is related the to rapid mechanical response rate of the piezo stack.

3.4.3. Velocity Field

Fig. 21 demonstrates the velocity field of the ammonia spray at various needle lift (35, 50, and 60 μm) at an injection pressure of 100 bar and a chamber pressure of 5 bar. It is clearly observed that a larger needle lift generates a larger velocity at the boundary of the spray. However, before the injector valve closing (0.588 ms ASOI), the optical flow method for velocity estimation might be not accurate due to the thick optical density. It shows that the velocity near the nozzle tip with 65 μm has the lowest velocity compared to the needle lift of 35 and 50 μm. This might be related the spray with larger needle lift has a denser region near the nozzle tip, which reduces the accuracy of the optical flow method. After the injector valve closing, the whole spray velocity field can be properly estimated. The spray with larger needle lift shows more velocity layers and more turbulence due to the increase of the momentum.

FIGURE 19 The spray penetration of ammonia at various needle lifts of 0.35, 0.50 and 0.65 µm

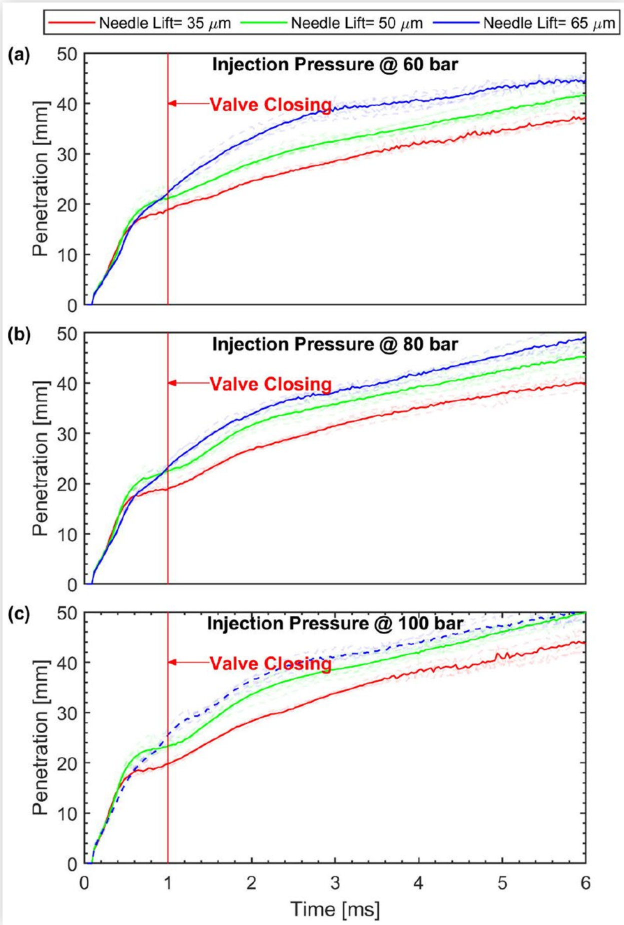

© Qiang Cheng, Aalto

FIGURE 20 The spray area of ammonia at various needle lifts of 0.35, 0.50 and 0.65 µm

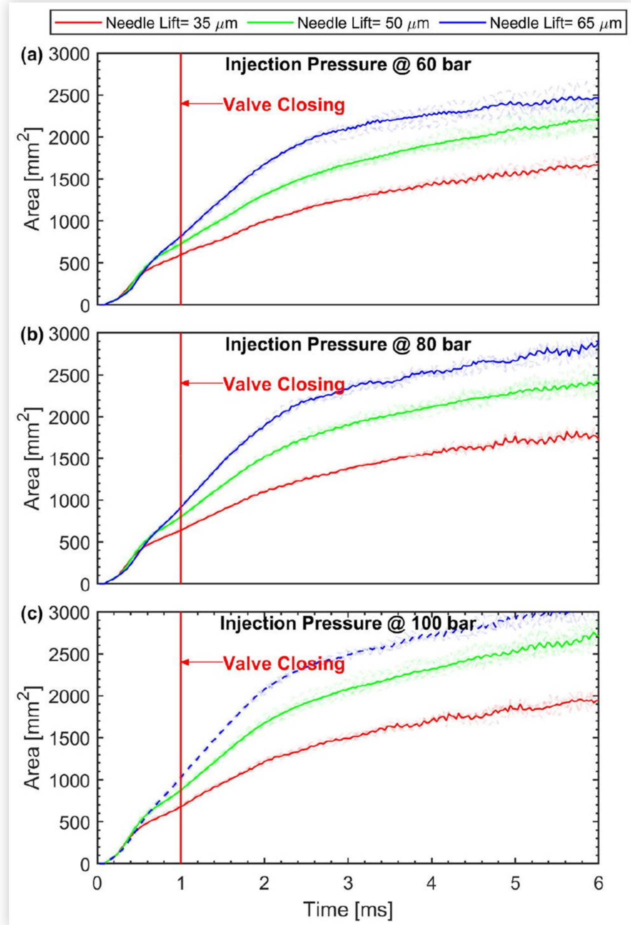

© Qiang Cheng, Aalto

3.5. Spray Characteristics of Various Renewable Fuels

In this section, effect of the fuel properties on the spray characteristic are investigated. Three renewable fuels ammonia, methanol, and ethanol sprays are studied for comparison. Fig. 22 shows the spray evolution of ammonia, methanol, and ethanol at an injection pressure of 100 bar and a chamber pressure of 5 bar. Fig. 22 shows that the large-scale motion takes place at the early stage of the spray development process. It can be observed that ammonia methanol and ethanol have different spray behaviour. Ammonia has very sharp boundary and small spray front at the beginning of the injection (< 0.294 ASOI). Then, a smooth boundary edge can be observed since the reduce of the velocity. However, methanol and ethanol show a flat spray front at the beginning of the injection ((< 0.294 ASOI). Then, a sharp boundary with many small spray fronts appeared. The sharp boundary edge is consistent until the 1.765 ms ASOI. The images also show that two vortexes can be clearly observed in ammonia spray, but no evident vortex can be observed in methanol and ethanol spray. Moreover, the evaporation of ammonia spray happens around 0.588 ms, which can be seen as lighter gaseous areas at the edges of the ammonia sprays especially in the last pictures. However, no evident vapor phase can be observed in methanol

FIGURE 21 Velocity field of ammonia spray at various needle lifts of 0.35, 0.50 and 0.65 µm

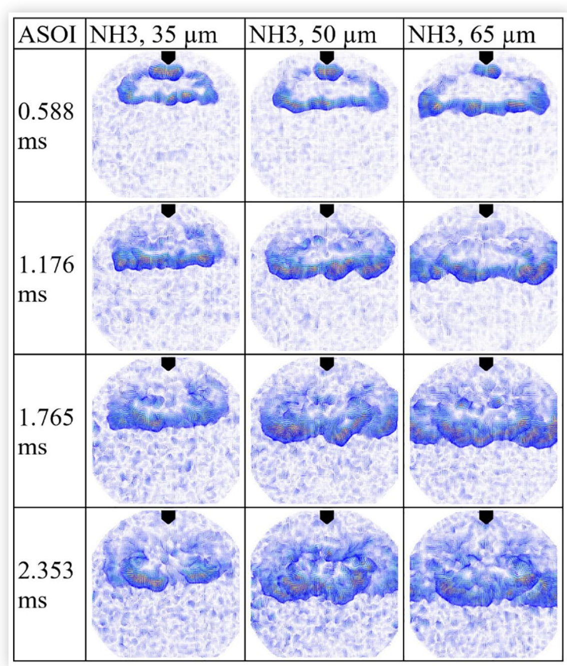

© Qiang Cheng, Aalto

FIGURE 22 Comparison of the spray volution of ammonia, methanol, and ethanol at an injection pressure of 100 bar and a chamber pressure of 5 bar

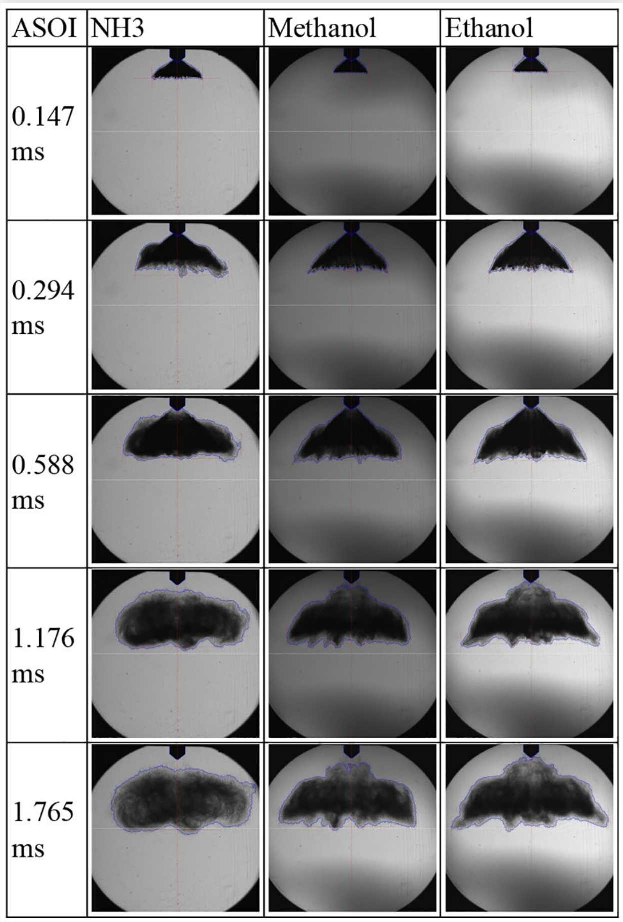

FIGURE 23 Comparison of the spray penetration of ammonia, methanol, and ethanol at an injection pressure of 100 bar and a chamber pressure of 5, 10 and 20 bar

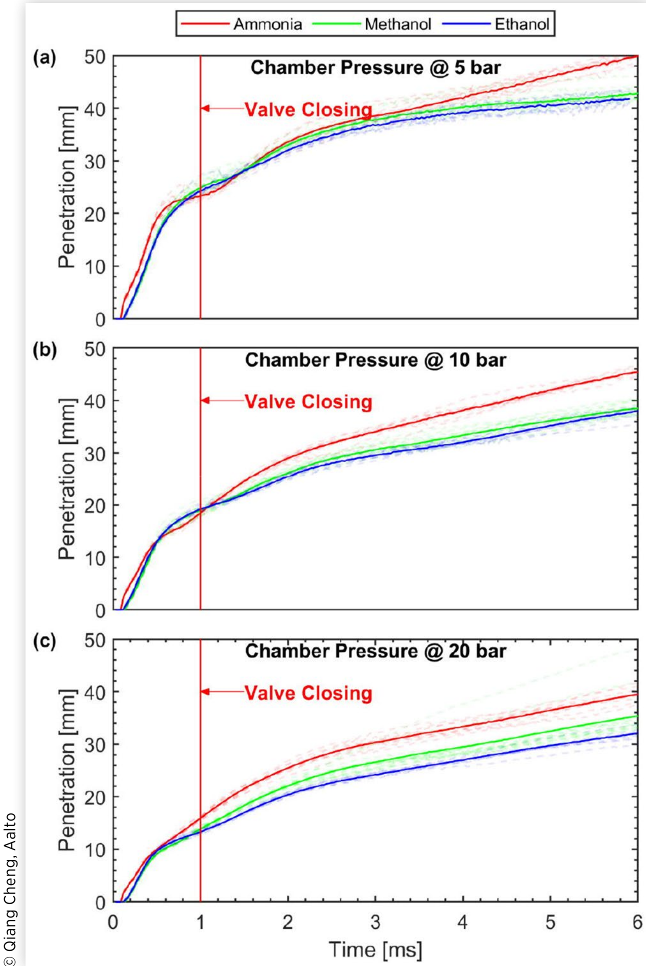

and ethanol sprays. The explanation is that ammonia has a lower viscosity and density than methanol and ethanol. Thus, the momentum of the ammonia spray is less than methanol and ethanol. Moreover, since the smaller molecular size of ammonia, resulting in a more sensitive to the air drag force. The appearance of the vapor phase in ammonia spray can be related to its higher vapor pressure (857.1 kPa @20 °C), which is much higher than methanol (13.02 kPa @20 °C) and ethanol (5.95 kPa @20 °C).

3.5.1. Spray Penetration Fig. 23 (a)-(c) demonstrates the comparison of the spray penetration of ammonia, methanol, and ethanol at an injection pressure of 100 bar and a chamber pressure of 5, 10, and 20 bar. It can be seen that before the injector valve closing, ammonia exhibits longer spray penetration compared to methanol and ethanol due to the lower density and viscosity. Methanol and ethanol present almost the same penetration. After the injector valve closing, an evident transition can be observed in ammonia penetration curves, especially at lower chamber pressure. However, there is no transition of the methanol and ethanol spray can be observed in penetration. This is because during the injector valve opening, the spray of the ammonia is more like liquid spray. However, after the injector valve closing, especially at lower chamber pressure (e.g., < 10 bar) the ammonia starts to evaporate and more like gas jet. It is interesting that the differences of penetration of methanol and ethanol is increased with the increasing of the chamber pressure after the injector valve closing. This is because the higher chamber pressure results larger air drag force, and it has more effects on the larger molecules.

3.5.2. Spray Area Fig. 24 (a)-(c) demonstrates the comparison of the spray area of ammonia, methanol, and ethanol at an injection pressure of 100 bar and a chamber pressure of 5, 10, and 20 bar. It can be seen that before the injector valve closing, the differences of the spray area of ammonia, methanol, and ethanol are recued with the increasing of the chamber pressure. However, after the injector valve closing, the differences of the spray area of ammonia, methanol, and ethanol are getting increased with the increasing of the chamber pressure. As explained in section 3.5.2, the higher chamber pressure results larger air drag force, and it has more effects on the larger molecules. The larger

FIGURE 24 Comparison of the spray area of ammonia, methanol, and ethanol at an injection pressure of 100 bar and a chamber pressure of 5, 10 and 20 bar

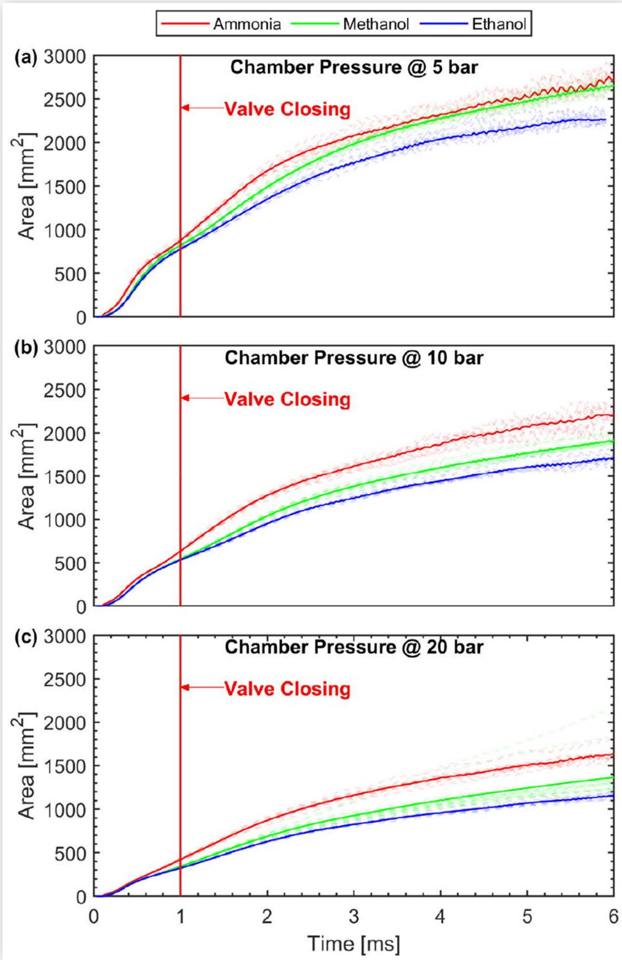

spray ammonia area also can be attributed to its lower density and viscosity, resulting in a larger initial jet velocity, which has longer penetration and larger spray area after start of injection. The results indicate that the ammonia shows better fuel-air mixing quality than methanol and ethanol. Since the larger area of the spray presents more effective mixing process.

3.5.3. Velocity Field Fig.25 depicts the comparison of the velocity field of ammonia, methanol, and ethanol at an injection pressure of 100 bar and a chamber pressure of 5 bar. It can be observed that the spray of the methanol shows higher velocity at the tip of the spray fronts. There are more spray fronts in the ethanol than methanol. As explained in previous sections, the air drag force has more effects on the larger molecules. Compared to the methanol and ethanol spray in the velocity field, the ammonia spray shows more even velocity at the spray front. Furthermore, at the end of the spray evolution (2.353ms ASOI), higher turbulence in the inner region of the ammonia spray can be observed. This is because the ammonia is evaporated during this time, and has more ammonia-air entrainments.

FIGURE 25 Comparison of the velocity field of ammonia, methanol, and ethanol at an injection pressure of 100 bar and a chamber pressure of 5 bar

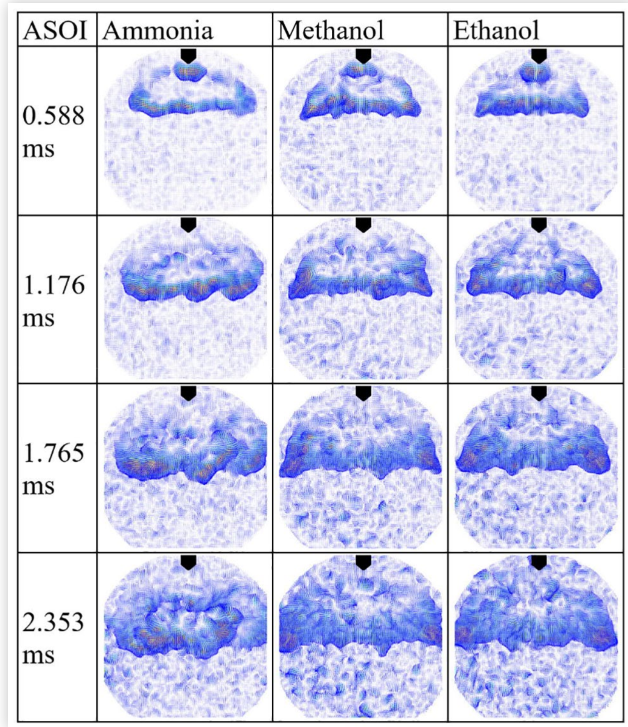

4. Summary/Conclusions

The present study focuses on ammonia spray characteristics of at various injection pressures (40, 60, 80 and 100 bar), chamber pressures (5, 10 and 20 bar), needle lift (35, 50, 65 μm). Additionally, the effect of the fuel properties on the spray characteristics are also investigated by comparing the spray behaviors of ammonia, methanol and ethanol. A high-speed schlieren imaging technique is implemented to capture the spray evolution. A novel optical flow method is applied to calculate the velocity field based on the schlieren images. The key findings from the present study are summarized below:

(1). Increasing the injection pressure leads to a longer spray penetration and larger spray area. The higher injection pressure also induces more turbulence in the spray.

(2). Contrary to the effect of injection pressure on the spray behaviours, increasing the chamber pressure results in a shorter spray penetration and smaller spray area. Since the increase of the chamber pressure leads to a higher chamber density and larger air drag force, which obstruct the spray propagation.

(3). The spray behaviour is the results of the combinative effect of injection pressure and chamber pressure. Therefore, the pressure ratio presents more sensitive to the spray characteristics. Generally, the same pressure ratio shows similar spray evolution in the liquid or gas fuels. However, this conclusion is not suitable to the ammonia due to the phase transition for the ammonia spray.

(4). The needle lift of the injector also shows dramatical effects on the ammonia spray characteristics. Since the increase of the needle lift leads to a larger injection rate and higher momentum. Therefore, increasing the needle lift results in a longer spray penetration and larger spray area.

(5). The comparison of the spray characteristics of ammonia, methanol and ethanol indicates that the spray penetration and area of ammonia is larger than those of methanol and ethanol due to its lower density and viscosity. Moreover, since the higher vapor pressure of the ammonia, it shows faster evaporation rate than methanol and ethanol. This implies that the ammonia spray has more effective fuel-air mixing process compared to methanol and ethanol.

References

1. IEA, *Energy Technology Perspectives 2020* (Paris: IEA, 2020)
2. Levinsky, H., "Why Can't We Just Burn Hydrogen? Challenges When Changing Fuels in an Existing Infrastructure," *Progress in Energy and Combustion Science* 84 (2021).
3. Valera-Medina, A., Xiao, H., Owen-Jones, M., David, W.I.F. et al., "Ammonia for Power," *Progress in Energy and Combustion Science* 69 (2018): 63-102 listed. Refer to the SAE Technical Paper Style Guide for formatting of different types of references. Apply the List-Ordered-Numeric style tag to format references. Below are some examples.
4. Lesmana, H., Zhang, Z., Li, X., Zhu, M. et al., "NH3 as a Transport Fuel in Internal Combustion Engines: A Technical Review," *ASME. J. Energy Resour. Technol.* 141, no. 7 (March 11, 2019): 070703. https://doi.org/10.1115/1.4042915.
5. Yapicioglu, A. and Dincer, I., "A Review on Clean Ammonia as a Potential Fuel for Power Generators," *Renewable and Sustainable Energy Reviews* 103 (2019): 96-108. https://doi.org/10.1016/j.rser.2018.12.023.
6. Zamfirescu, C. and Dincer, I., "Ammonia as a Green Fuel and Hydrogen Source for Vehicular Applications," *Fuel Process Technol* 90 (2009): 729-737, doi:10.1016/j.fuproc.2009.02.004.
7. Boggs, B.K. and Botte, G.G., "On-Board Hydrogen Storage and Production: An Application of Ammonia Electrolysis," *J. Power Sources* 192 (2009): 573-581, doi:10.1016/j.jpowsour.2009.03.018.
8. Uribe, F.A. et al., *J. Electrochem. Soc.* 149 (2002): A293.
9. Ganley, J.C., "An Intermediate-Temperature Direct Ammonia Fuel Cell with a Molten Alkaline Hydroxide Electrolyte," *J. Power Sources* 178 (2008): 44-47, doi:10.1016/j.jpowsour.2007.11.093.
10. Yang, J., Muroyama, H., Matsui, T., and Eguchi, K., "Development of a Direct Ammonia-Fueled Molten Hydroxide Fuel Cell," *J. Power Sources* 245 (2014): 277-282, doi:10.1016/j.jpowsour.2013.06.143.
11. Fuerte, A., Valenzuela, R.X., Escudero, M.J., and Daza, L. (2009). Ammonia as Efficient Fuel for SOFC. *Journal of Power Sources*, 192(1), 170-174. https://doi.org/10.1016/J.JPOWSOUR.2008.11.037
12. Afif, A., Radenahmad, N., Cheok, Q., Shams, S. et al., "Ammonia-Fed Fuel Cells: A Comprehensive Review," *Renewable and Sustainable Energy Reviews* 60 (2016): 822-835. https://doi.org/10.1016/j.rser.2016.01.120.
13. Dimitriou, P. and Javaid, R., "A Review of Ammonia as a Compression Ignition Engine Fuel," *International Journal of Hydrogen Energy* 45, no. 11 (2020): 7098-7118. https://doi.org/10.1016/j.ijhydene.2019.12.209.
14. Erdemir, D., Dincer, I.. A Perspective on the Use of Ammonia as a Clean Fuel: Challenges and Solutions. *Int J Energy Res.* 2021; 45: 4827- 4834. https://doi.org/10.1002/er.6232
15. Starkman, E., Newhall, H., Sutton, R., Maguire, T. et al., "Ammonia as a Spark Ignition Engine Fuel: Theory and Application," SAE Technical Paper 660155, 1966, https://doi.org/10.4271/660155.
16. Starkman, E., James, G., and Newhall, H., "Ammonia as a Diesel Engine Fuel: Theory and Application," SAE Technical Paper 670946, 1967, https://doi.org/10.4271/670946.
17. Sawyer, R., Starkman, E., Muzio, L., and Schmidt, W., "Oxides of Nitrogen in the Combustion Products of an Ammonia Fueled Reciprocating Engine," SAE Technical Paper 680401, 1968, https://doi.org/10.4271/680401.
18. Starkman, E.S., James, G.E., and Newhall, H.K., "Ammonia as a Diesel Engine Fuel: Theory and Application," *SAE Transactions* 76 (1968): 3193-3212. http://www.jstor.org/stable/44562852.
19. Cooper, J.R., Crookes, R.J., Rose, J.W., and Mozafari, A. "Ammonia as a Fuel for the IC Engine," Switzerland: N. p., 1991. Web.
20. Toyota, Asian Industries, 2010. https://www.toyota-industries.com/investors/library/annual_reports/2010/.
21. Pearsall, T. and Garabedian, C., "Combustion of Anhydrous Ammonia in Diesel Engines," SAE Technical Paper 670947, 1967, https://doi.org/10.4271/670947.
22. Koike, M. and Suzuoki, T., "In-Line Adsorption System for Reducing Cold-Start Ammonia Emissions from Engines Fueled with Ammonia and Hydrogen," *International Journal of Hydrogen Energy* 44, no. 60 (2019): 32271-32279, ISSN 0360-3199. https://doi.org/10.1016/j.ijhydene.2019.10.105.
23. Cheng, Q., Zhang, Z., and Xie, N., "Power Losses and Dynamic Response Analysis of Ultra-High Speed Solenoid Injector Within Different Driven Strategies," *Applied Thermal Engineering* 91 (2015): 611-621. https://doi.org/10.1016/j.applthermaleng.2015.08.053.
24. Zhang, Z., Zhang, W., Ma, X., Awad, O.I. et al., "Effects of GDI Injector Deposits on Spray and Combustion Characteristics Under Different Injection Conditions," *Fuel* 278 (2020): 118094. https://doi.org/10.1016/j.fuel.2020.118094.
25. Muddapur, A., Jose, J.V., Sahu, S., and Sundararajan, T., "Spray Dynamics and Evaporation in a Multihole GDI Injector for Pulsatile and Split Injection at Elevated Ambient

Pressure and Temperature Conditions," *Fuel* 279 (2020): 118057. https://doi.org/10.1016/j.fuel.2020.118057.

26. Park, S.H., Kim, H.J., Suh, H.K., and Lee, C.S., "Atomization and Spray Characteristics of Bioethanol and Bioethanol Blended Gasoline Fuel Injected Through a Direct Injection Gasoline Injector," *International Journal of Heat and Fluid Flow* 30, no. 6 (2009): 1183-1192. https://doi.org/10.1016/j.ijheatfluidflow.2009.07.002.
27. Chang, M., Park, J., Kim, B., Park, J.H. et al., "Effect of Sac-Volume on the Relationship Among Ball Behavior, Injection and Initial Spray Characteristics of Ultra-High Pressure GDI Injector," *Fuel* 285 (2021): 119089. https://doi.org/10.1016/j.fuel.2020.119089.
28. Sun, Z., Cui, M., Ye, C., Yang, S. et al., "Split Injection Flash Boiling Spray for High Efficiency and Low Emissions in a GDI Engine Under Lean Combustion Condition," *Proceedings of the Combustion Institute* 38, no. 4 (2021): 5769-5779. https://doi.org/10.1016/j.proci.2020.05.037.
29. Sharma, N. and Agarwal, A.K., "Macroscopic Spray Characteristics of a Gasohol Fueled GDI Injector and Impact on Engine Combustion and Particulate Morphology," *Fuel* 295 (2021): 120461. https://doi.org/10.1016/j.fuel.2021.120461.
30. Gong, C., Si, X., and Liu, F., "Effects of Injection Timing and CO2 Dilution on Combustion and Emissions Behaviors of a Stoichiometric GDI Engine Under Medium Load Conditions," *Fuel* 303 (2021): 121262. https://doi.org/10.1016/j.fuel.2021.121262.
31. Lefebvre, A.H., Wang, X.F., and Martin, C.A., "Spray Characteristics of Aerated-Liquid Pressure Atomizers," *Journal of Propulsion and Power* 4 (1988): 293-298.
32. Cavicchi, A. and Postrioti, L., "Simultaneous Needle Lift and Injection Rate Measurement for GDI Fuel Injectors by Laser Doppler Vibrometry and Zeuch Method," *Fuel* 285 (2021): 119021. https://doi.org/10.1016/j.fuel.2020.119021.
33. Zengyang, W., Wang, L., Badra, J.A., Roberts, W.L. et al., "GDI Fuel Sprays of Light Naphtha, PRF95 and Gasoline Using a Piezoelectric Injector Under Different Ambient Pressures," *Fuel* 223 (2018): 294-311. https://doi.org/10.1016/j.fuel.2018.03.009.
34. Wang, L., Zengyang, W., Badra, J.A., Roberts, W.L. et al., "Soot Characteristics of High-Reactivity Gasoline Under Compression-Ignition Conditions Using a Gasoline Direct Injection (GDI) Piezoelectric Fuel Injector," *Fuel* 265 (2020): 116931. https://doi.org/10.1016/j.fuel.2019.116931.
35. Komada, K. and Moon, S., "Transient Needle Motion of an Outwardly Opening GDI Injector and Its Effects on Initial Spray Formation," *Fuel* 181 (2016): 964-972. https://doi.org/10.1016/j.fuel.2016.05.012.
36. Jianguo, D., Cenker, E., Badra, J., Sim, J. et al., "Characteristics of a Non-Reacting Spray from an Outwardly Opening Hollow-Cone Injector with High-Reactivity Gasolines," *Fuel* 268 (2020): 117293. https://doi.org/10.1016/j.fuel.2020.117293.
37. Achleitner, E., Bäcker, H., and Funaioli, A., "Direct Injection Systems for Otto Engines," 2007.
38. Skogsberg, M., Dahlander, P., and Denbratt, I., "Spray Shape and Atomization Quality of an Outward-Opening Piezo Gasoline DI Injector," SAE Technical Paper 2007-01-1409, 2007, https://doi.org/10.4271/2007-01-1409.
39. Wang, L., Badra, J.A., Roberts, W.L., and Fang, T., "Characteristics of Spray from a GDI Fuel Injector for Naphtha and Surrogate Fuels," *Fuel* 190 (2017): 113-128.
40. Wu, Z., Wang, L., Badra, J.A., Roberts, W.L. et al., "GDI Fuel Sprays of Light Naphtha, PRF 95 and Gasoline Using a Piezoelectric Injector Under Different Ambient Pressures," *Fuel* 223 (2018): 294-311.
41. Wang, L., Wang, F., and Fang, T., "Flash Boiling Hollow Cone Spray from a GDI Injector Under Different Conditions," *International Journal of Multiphase Flow* 118 (2019): 50-63. https://doi.org/10.1016/j.ijmultiphaseflow.2019.05.009.
42. Raffel, M., Willert, C., Wereley, S., and Kompenhans, J., *Particle Image Velocimetry* (Berlin, Germany: Springer, 2007)
43. Adrian, R.J. and Westerweed, J., *Particle Image Velocimetry* (Cambridge, UK: Cambridge University Press, 2011)
44. Stanislas, M., Okamoto, K., and Kähler, C., "Main Results of the First International PIV Challenge," *Meas Sci Technol* 14 (2003): R63-R89.
45. Stanislas, M., Okamoto, K., Kähler, C., and Westerweel, J., "Main Results of the Second International PIV Challenge," *Exp Fluids* 39 (2005): 170-191.
46. Stanislas, M., Okamoto, K., Kähler, C., and Westerweel, J., "Scarano F, Main Results of the Third International PIV Challenge," *Exp Fluids* 45 (2008): 27-71.
47. Liu, T. and Shen, L., "Fluid Flow and Optical Flow," *J Fluid Mech* 614 (2008): 253-291.
48. Heitz, D., Memin, E., and Schnorr, C., "Variational Fluid Flow Measurements from Image Sequences: Synopsis and Perspectives," *Exp Fluids* 48 (2010): 369-393.
49. Quenot, G.M., Pakleza, J., and Kowalewski, T.A., "Particle Image Velocimetry with Optical Flow," *Exp Fluids* 25 (1998): 177-189.
50. Ruhnau, P., Kohlberger, T., Schnorr, C., and Nobach, H., "Variational Optical Flow Estimation for Particle Image Velocimetry," *Exp Fluids* 38 (2005): 21-32.
51. Yuan, J., Schnorr, C., and Memin, E., "Discrete Orthogonal Decomposition and Variational Fluid Flow Estimation," *Journal of Mathematical Imaging and Vision* 28 (2007): 67-80.
52. Corpetti, T., Memin, E., and Perez, P., "Dense estimation of fluid flows IEEE Trans on Pattern Analysis and Machine," *Intelligence* 24 (2002): 365-380.
53. Wang, B., Cai, Z., Shen, L., and Liu, T., "An Analysis of Physics-Based Optical Flow Method," *J Comp Appl Math* 276 (2015): 62-80.
54. Chen, L., Li, G., Huang, D., Zhang, Z. et al., "Experimental and Numerical Study on the Initial Tip Structure Evolution of Diesel Fuel Spray Under Various Injection and Ambient Pressures," *Energy* 186 (2019): 115867. https://doi.org/10.1016/j.energy.2019.115867.
55. Gerold, J., Vogl, P., and Pfitzner, M., "New Correlation of Subsonic, Supersonic and Cryo Gas Jets Validated by Highly Accurate Schlieren Measurements," *Exp Fluids* 54 (2013): 1542.

Contact Information

Qiang Cheng
Puumiehenkuja 5A, 02150 Espoo, Finland
Department of Mechanical Engineering
Aalto University
qiang.cheng@aalto.fi

Acknowledgments

Financial support from Aalto University, School of Engineering (Department of Mechanical Engineering) and Finnish Academy project (Grant No. 297248) is gratefully acknowledged.

e-ISSN 2641-9645